Hardware and software design for a National Instrument-based magnetic induction tomography system for prospective biomedical applications

Hardware and software design for a National Instrument-based magnetic induction tomography system for prospective biomedical applications

Hsin-Yu Wei and Manuchehr Soleimani

Department of Electronics and Electrical Engineering, University of Bath, Bath, UK

E-mail: m.soleimani@bath.ac.uk

Abstract

Magnetic induction tomography (MIT) is a new and emerging type of tomography technique that is able to map the passive electromagnetic properties (in particular conductivity) of an object. Excitation coils are used to induce eddy currents in the medium, and the magnetic field produced by the induced eddy current is then sensed by the receiver coils. Because of its non-invasive and contactless feature, it becomes an attractive technique for many applications (especially in biomedical area) compared to traditional contact electrode-based electrical impedance tomography. Due to the low contrast in conductivity between biological tissues, an accurate and stable hardware system is necessary. Most MIT systems in the literature employ external signal generators, power amplifiers and highly stable down-conversion electronics to obtain a satisfactory phase measurement. However, this would increase design complexity substantially. In this paper, a National Instrument-based MIT system is developed at the University of Bath, aiming for biomedical applications. The system utilizes National Instrument products to accomplish all signal driving, switching and data acquisition tasks, which ease the system design whilst providing satisfactory performance. This paper presents a full-scaled medical MIT system, from the sensor and system hardware design, eddy current model verification to the image reconstruction software: the performance of this MIT instrumentation system is characterized in detail, including the system accuracy and system stability. The methods of solving eddy current problem are presented. The reconstructed images of detecting the presence of saline solutions are also included in this paper, which show the capability of national instrument products to be developed into a full-scaled biomedical MIT system, by demonstrating the practical experimental results.

Keywords: magnetic induction tomography, inverse eddy current, problem, FPGA-based MIT system

(Some figures may appear in colour only in the online journal)

1. Introduction

Magnetic induction tomography (MIT) is one of the electrical tomography techniques that images the spatial distribution of electrical conductivity and magnetic permeability inside a region of interest. Its contactless imaging feature makes it potentially more attractive for biomedical and some other industrial non-destructive testing applications. For a typical MIT system, coils are used as the transmitters and receivers based on the mutual inductance theory. By establishing a sinusoidal current into the transmitting coils, a changing magnetic flux is set up, which induces a voltage across the terminals of sensor coils. This induced signal magnetic field strength, B, is often referred to as the 'background' signal (Griffiths 2001). If an object is positioned between two coils, eddy current will be induced on the object. This eddy current can produce a secondary magnetic field, which will induce a 'secondary voltage signal $\triangle B$' and perturb the background signal at the receiving coil. The magnitude of this perturbation is proportional to the object's conductivity.

In biomedical applications, due to the low-conductivity features ($\sigma < 3$ S m^{-1}) of the measuring samples (Griffiths 2001, Scharfetter *et al* 2001), the magnitude of signal perturbation is several orders less than the acquired signal in industrial applications, which generally monitor high-conductivity materials ($\sigma > 10^6$ S m^{-1}) such as metal. The signal perturbation induced by biological samples is generally <1%, and increases in proportion to the driving frequency and tissue conductivity. For biological applications, the perturbation is mainly dominated by the phase shift, i.e. Im($\triangle B/B$), which contains the information required for image reconstruction (Griffiths 2001). Due to the small perturbation, a highly accurate and stable signal source and phase shift measurement hardware are necessary for an MIT system. In the literature, most of the MIT hardware relies on external signal generators and power amplifiers to ensure a low-noise, high-power driving signal (Patz *et al* 2010, Watson *et al* 2011, McEwan *et al* 2009, Wee *et al* 2008). Using many external devices could potentially add significant complexity to system design and hardware synchronization. If the heterodyne technique is also implemented (Vauhkonen *et al* 2008, McEwan *et al* 2009, Watson *et al* 2003), an extra IF signal source will be required for signal down conversion, which can be more problematic.

In this paper, an NI-based system for biomedical MIT applications is presented. The aim of the proposed system is to utilize National Instruments (NI) products and LabView to centralize the driving, switching and measuring tasks of the MIT system, which decreases the system design complexity and eliminates the synchronization problem completely. The performance of the phase detection of our system is carried out with the following parameters: phase linearity, phase noise (with respect to different input levels) and phase drift. Two phase measurement techniques in LabView (FFT tone measurement and quadrature demodulation) are also compared to decide which technique will be implemented to perform the phase measurement for the later saline solution experiment. The initial system performance result is satisfactory, and can be compared with the result reported in Patz *et al* (2010).

With a complete 16-channel setup (eight transmitters and eight receivers), a full set of the measured data can be collected. Transferring the voltage measurements to the reconstructed images (inverse problem) requires solving the forward model and inverse problems numerically using finite element method (FEM). In the literature of electromagnetic analysis in MIT, meshing the complex shaped coils as part of discretization within the imaging domain is essential (Soleimani *et al* 2005, Soleimani 2006, Soleimani and Lionheart 2005). However, this discretization process decreases both the flexibility of the forward model and efficiency of the inverse solver. In this paper, a two-potential technique is implemented in the MIT forward solver, which means the coils can be defined independently from the mesh, and the coil mesh is no longer necessary in the FEM model (Biro and Preis 1989, Biro 1999, Kameari 2004).

This paper conducts a fully integrated biomedical MIT system, from the initial hardware development (coil sensor and NI LabView program) to software model (complete eddy current problem analysis in MIT and inverse solver). After solving the forward and inversion problems, the reconstructed images from the real sample experiments are also provided and discussed in section 5.

2. Front-end sensor design

Various types of coils have been used for MIT systems, including air-core coils and gradiometers (Korjenevsky *et al* 2000, Scharfetter *et al* 2005, Rosell-Ferrer *et al* 2006). From the literature, it is known that minimizing the capacitive coupling between the transmitting and receiving coils is an essential task for the coil designing process, as this unwanted capacitive coupling can easily be greater than the true magnetic coupling signal. Several methods were reported to minimize the direct capacitive coupling (Griffiths *et al* 2007, Wei and Wilkinson 2011, Watson *et al* 2001, Scharfetter *et al* 2001).

A hand-wound air-core coil was selected for the MIT system because of its linear behaviour. E-field shielding, individual coil screening and balanced coil configurations were implemented in the sensor structure for internal/external electric field screening. A grounded aluminium cylinder was used to cover the entire imaging system to prevent the external E-field perturbation. The individual coil screening was accomplished by constructing the coil using screened audio cable. The screen was grounded at one point only to avoid magnetically induced current in the screen. Balanced configuration was also implemented to not only provide some rejection of the common mode capacitive coupling at the receiver side, but also maximize the driving current at the transmitter side. Both the use of screened cable and the balanced coil structure were found very useful to eliminate the capacitive coupling. The details of the screening methods are described in Wei and Wilkinson (2011).

The coils should operate at a frequency below the resonance to obtain the inductor behaviour. It was also reported that a very rapid change in measured phase is observed when operating under resonance (Watson 2009), showing that resonance frequency can cause instability of the phase measurement system.

The inductance and corresponding input impedance of the coil at the operational frequency are important factors to determine the appropriate number of turns. If the number of turns is too few, there will not be enough inductance and the magnetic flux will be too low to induce voltage at the receiver; if the number of turns is too many, the coil resonance frequency may be too close to the operational frequency. In our MIT system, a six-turn balanced coil was selected; the number was decided empirically based on the sensor performance over the phase measurement experiments. The balanced sensor was constructed onto a 4 cm diameter plastic cylindrical former, which provided a resonance frequency of 45 MHz, with a low inductance of 1.8 μH.

Additional electronics are normally required between the sensors and the NI instrumentation devices for the buffering purposes. One of the advantages of choosing the balanced sensor structure is to enlarge the driving signal by combining the sensor with a differential amplifier. A fully differential amplifier THS4500 was selected to amplify the transmitting output amplitude from 0.5 Vp–p single-ended to 8 Vp–p differential signal, so that the magnetic flux strength and phase stability could be improved. For the receivers, a low-noise, high-speed amplifier THS4275 was used to buffer the receiving signals. THS4275 was chosen because of its wide bandwidth, high slew rate and low-voltage noise which could again assure the phase measurement stability. The typical differential to single-ended conversion circuit was implemented in the receiving circuits, with resistor values for input resistor and

feedback resistor of 1.1 and 22 kΩ, respectively. Although it is later reported in Watson *et al* (2011) that THS4275 chips do not have a good temperature coefficient, all our experiments are going to be conducted under a temperature-controlled environment in order to maintain the optimal performance.

3. NI system setup and performance

For medical application MIT systems, the sensitivity of the coils is going to degrade significantly due to the extremely small conductivity of measuring samples; hence, a very accurate measurement system is required. In this section, we explain the key criteria for selecting 'off-the-shelf' NI hardware devices for our MIT system. The following system requirements were considered when choosing the NI devices:

- For system flexibility and future spectral imaging expansion, the devices need to generate the transmitting signal with a wide range of frequencies (kHz to MHz) since different target measuring materials will have different optimal operating frequencies.
- A high-speed direct digitization device will be required for taking measurements from receiving coils. Direct digitization here is defined as analogue–digital conversion of the high-frequency signal without down converting the signal into a lower frequency range. Direct digital sampling eliminates the mixing process and therefore fewer electronic components are required. It also provides better flexibility for future modifications.
- The devices need to be capable of expanding the system into a multi-channel MIT system.

Based on the considerations above, a high-speed MIT system was constructed based on the following devices: NI 2593, NI 5781 and NI 7951. NI 5781 is a 40 MHz baseband transceiver that contains dual 100 MS s^{-1}, 14 bits, differential, dc-coupled ADC analogue inputs (AI) and dual 100 MS s^{-1}, 16 bits, differential, dc-coupled DAC analogue outputs (AO). Its 100 MS s^{-1} ADC/DAC provide us a wide choice of operating frequencies, ranges from few kHz to maximum of 20 MHz. NI 2593 is a 500 MHz $2 \times 8 : 1$ multiplexer that controls all the channel switching tasks for the system.

Using a centralized NI system has a drawback: long downloading and processing time (Patz *et al* 2010). For this reason the NI 5781/7951 combination was selected. The 7951 FlexRIO board contains a LabView programmable FPGA module; its direct memory access architecture allows high-speed data streaming, which can speed up the data acquisition process. Data acquisition time could potentially be decreased further if the mathematical libraries of the LabView FPGA were implemented, i.e. performing signal processing tasks using the FPGA chip. However this implementation will become the future work of the project. Some of the latest reported MIT systems were also constructed based on FPGA chips, such as Cardiff Mk2 system (Patz *et al* 2010) and some industrial MIT systems (Yin *et al* 2011).

3.1. System characterization setup

The NI-based measurement system setup is shown in figure 1. AO-Ch0 is connected to AI-Ch0 and AO-Ch1 is connected to AI-Ch1. AO-Ch0 generates the variable driving signal, whose amplitude and phase can be altered for system characterization. AO-Ch1 is the reference signal source, whose amplitude is fixed to 1 V and is directly fed into AI-Ch1 for the phase and amplitude calculations.

In this system setup, the driving frequency is fixed to 10 MHz. With a 100 MS s^{-1} sampling frequency, a 40 MHz, seventh-order elliptical low-pass filter is necessary at each DAC output for smoothing the sinusoidal signals. The NI 7951 Flex-RIO device provides a
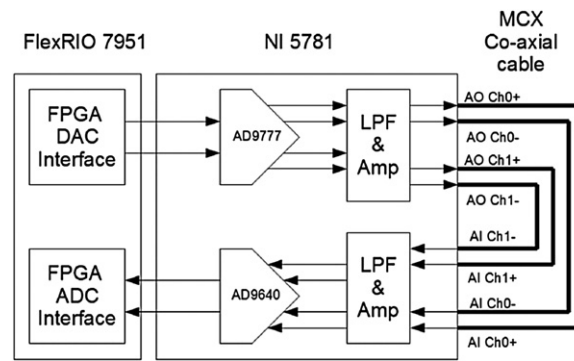
Figure 1. Block diagram of the system setup.

fast platform for data acquisition and signal processing. The dual 5781 ADC inputs sample the 10 MHz signal simultaneously with a 100 MS s^{-1} sampling rate. There are no other electronics involved in this setup, so the performance of the system is completely dependent on the NI devices. Under each trigger, the FPGA will sample 8192, 14-bit measurements from the NI-5781 inputs. These samples are then used to calculate the phase and amplitude of the receiving signals.

After the sampling, the FPGA chip will transfer all the measurement to the work station for signal processing. The data processing tasks are all accomplished in LabView. In LabView, two phase measuring algorithms are used for comparison: FFT tone measurement and I/Q demodulation. FFT tone measurement is a LabView built-in function, which can compare the tone information (amplitude and phase difference) between the driving and the receiving signals using FFT analysis. In the other case, I/Q demodulation uses the reference signal obtained from AI-CH1 to produce its own quadrature (I/Q) signals by passing the reference signal through a third-order Butterworth filter (90° phase shift). The receiving signal sampled by AI-CH0 is then multiplied with the stored I/Q signal to give us the phase and amplitude measurements. In the next sections, direct tone measurement and I/Q demodulation will be evaluated to decide which method can offer better measuring qualities.

With the configuration shown in figure 1, three parameters were characterized to evaluate the hardware performance: phase linearity, phase noise and phase drift. The characterization process and results are discussed in the next sections.

3.2. Phase linearity

To test the phase linearity, the phase difference between the driving signal and the reference signal was varied in LabView from 1 to 100 millidegrees. The driving frequency was set to 10 MHz. 20 phase measurements (6 ms time constant) were averaged to determine the phase. The linearity performance is shown in figure 2. However, the figure shows only the phase linearity result from 1 to 40 millidegrees, as for a biomedical MIT system we want our phase measurement accuracy to be within millidegree ranges. The phase measurements were obtained by FFT tone measurement and I/Q demodulation. A linear regression model was applied to both results in order to find the linearity between the actual and measured phase difference.

The correlation coefficient (R^2) values were calculated using the linear regression model: 0.9997 and 0.9996 for FFT measurement and I/Q demodulation, respectively, i.e. the FFT
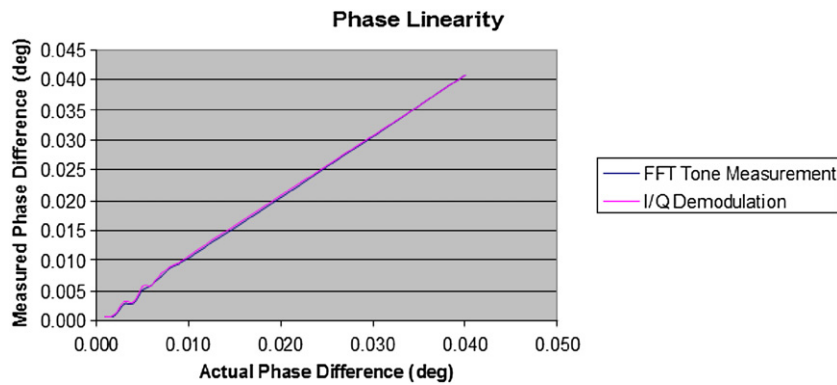
Phase Linearity

Figure 2. Phase linearity—relationship between the actual and measured phase difference.

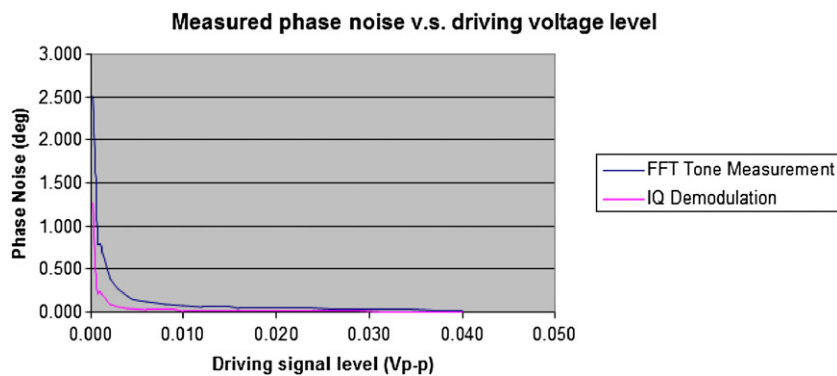**Measured phase noise v.s. driving voltage level**

Figure 3. Measured phase noise versus the driving signal level.

tone measurement had a slightly better phase measurement linearity. The nonlinearity was observed in both cases when only a small amount of phase shift was introduced into the driving signal. Apart from the ADC's performance, the limitation of the DAC's digital data range was also believed to be one of the reasons causing nonlinearity. The linearity result can be more accurate if the number of steps in the DDS lookup table are increased. The system's linearity performance is slightly worse than the $R^2 = 0.9998$ performance in Patz *et al* (2010).

3.3. Phase noise versus signal input level

The phase noise was measured by calculating the standard deviation of the phase measurement over a period of time. In this case, the phase noise measurements were measured against the driving voltage level. The driving level was varied from 0.2 to 40 mV. The driving frequency was still 10 MHz. 50 phase measurements (6 ms time constant) were used to calculate the standard deviation (phase noise). Figure 3 shows the results from the tone measurement and I/Q demodulation.

For the same driving level, it shows that the I/Q demodulation technique offers much better noise stability than FFT tone measurements. At the 40 mV input level, the phase noise for quadrature and FFT methods is 0.004°, which is more stable than the 0.0075° noise
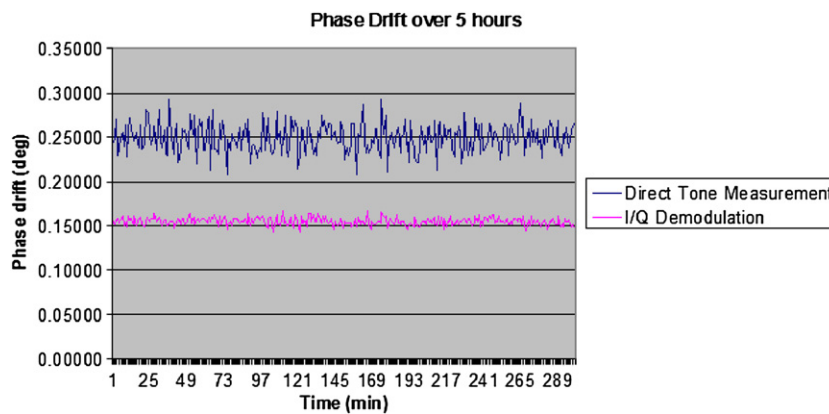
Figure 4. Phase drift measurement over a period of 300 min.

performance in Patz *et al* (2010). The experiment also indicates that the driving signal needs to be maximized to ensure a better phase noise performance.

3.4. Phase drift

Phase drift is also known as the system's long-term stability. The phase was measured every minute for 5 h. The phase drift was defined as the difference between the initial measured phase value and the later phase measurement. Again, a 10 MHz, 50 mV driving signal was used. Different phase offsets were introduced between the driving and reference signals to help in visualizing the phase drift result, which is shown in figure 4.

The phase drift result corresponds with the previous phase noise measurements. The direct tone measurement had a larger fluctuation than the I/Q demodulation. The maximum difference observed for tone measurement was 85 millidegrees over a period of 5 h. Under the same conditions, only 25 millidegree difference was observed from the I/Q technique. Compared to the phase drift result shown in Patz *et al* (2010), the observed phase drift is considered to be very low since all of the system mechanisms are properly designed, such as hardware chassis and cooler fan. These mechanisms can effectively protect the data acquisition system from external perturbations like temperature variation. Hence, the long-term stability of the system's phase measurement can be enhanced. The advantages of using NI products can be seen here in this experiment.

The study in section 3 has shown a preliminary characterization for our NI-based MIT system. From the system performance result, it can be seen that the NI devices are capable of measuring phase difference in millidegree ranges, provided that the detected signal is large enough. Furthermore, it is noted that the quadrature (I/Q) demodulation method offers much better measurement stability than the FFT tone measurement technique, and FFT tone measurement has a slightly better phase linearity performance.

To give a better picture of the state of the art of the MIT system hardware, the system information for the recently developed MIT systems is compared: Bath Medical Systems, Cardiff Mk2 System (Patz *et al* 2010, Watson *et al* 2008), Graz Mk2 System (Scharfetter *et al* 2008), Philips Research System (Vauhkonen *et al* 2008, McEwan *et al* 2009) and the Glamorgan System (Watson *et al* 2003). The comparison results are summarized and shown in table 1.

Table 1. Comparison of the recently developed MIT systems.

	Bath Medical System	Cardiff Mk2 System	Graz Mk2 System	Philips Research System	Glamorgan System
Operational Frequency and Coil Resonance	10 MHz, Resonance: 45 MHz	10 MHz Resonance: over 50 MHz	50 kHz − 1.5 MHz Resonance: 1.56 MHz	10 MHz	10 MHz
Sampling Rate (Samples/sec)	100 MS/s	120 MS/s	60 MS/s	192 kS/s (for the down converted 10 kHz signal)	No ADC (1GHz Oscilloscope)
Driving Level	8 Vp-p (Approx. 30 mA)	Approx. 100 mA rms	Maximum 200 mA can be achieved when freq. = 1 MHz	1.7 V rms 50 mA rms	8 Vp-p (no current information)
Phase Noise (m°)	4 m° (with 40 mV input level)	9 m° (with 40 mV input level)	N/A	Max 12.5 m° Min 2.2 m° (200 mA driving level)	N/A No reading is provided
Phase Drift (m°)	Max. drift of 25 m° over 5 hours (50 mV p-p input level)	Max. drift of 119 m° over 6 hours (65 mV rms input level)	N/A	102 m° over 30 mins (200 mA at driving coil)	27 m° over 20 mins (-21 dBV input level)
System Linearity	R²=0.9996 (Linearity w.r.t input level)	R²=0.9998 (Linearity w.r.t input level)	N/A	R²=0.9878 (Linearity w.r.t conductivity)	N/A

4. Experimental setup

4.1. Eddy current model for MIT

The purpose of solving the forward problem is to calculate the measurement signals for a predefined conductivity distribution. In MIT, the forward problems are mainly comprised by the eddy current problems, which are governed by Maxwell's equations. The numerical analysis of eddy current problems with the aid of FEM has become the primary method in recent decades. However, in Soleimani *et al* (2005), Soleimani (2006), discretizing the coil structures into the FEM mesh model is necessary. This discretization process increases the difficulty and complexity of the mesh model; moreover, the system becomes very inflexible due to the restriction from the size and the location of the coil sensors.

The method to avoid this is to define two potentials (freespace potential and reduced potential) in different mesh regions using the Biot–Savart theory. In this case, coils can be defined separately from the mesh and no coil discretization will be required. In this case, the accuracy of the Biot–Savart integration becomes very important for ensuring the divergence of the eddy current solution (Kameari 2004). In the (A, A) formulation by edge FEM, A_s in the freespace can be defined using the Biot–Savart law

$$B_s = \int \frac{\mu_0}{4\pi} \frac{I \mathrm{d}l \times r}{|r|^3}, \tag{1}$$

$$B_s = \nabla \times A_s, \tag{2}$$

where I is the source current, dl is a vector whose magnitude is the length of the differential element of the wire, μ_0 is the freespace permeability constant and B_s is the integration of the magnetic field along each source current segment. This freespace A_s is defined based on the scale of the designed 16-channel MIT system. On the other hand, the reduced potential A_e is the potential inside the eddy current region which includes the gradient of the electric scalar potential

$$\nabla \times (\mu^{-1}\nabla \times A_e) + j\omega\sigma A_e = J_s, \tag{3}$$

where σ is the conductivity distribution within the eddy current domain, ω is the operational frequency and J_s on the right-hand side is the current density in the excitation coil which can be defined based on the freespace components A_s and B_s.

$$\nabla \times (\mu^{-1}\nabla \times A_e) + j\omega\sigma A_e = \nabla \times H_s - \nabla \times \frac{\mu_0}{\mu}H_s - j\omega\sigma A_s. \tag{4}$$

This eddy current equation (equation (4)) can be applied into Galerkin's approximation using edge element basis function (Biro and Preis 1989, Biro 1999, Biro and Preis 2000). Galerkin's approximation yields

$$\int_{\Omega_e} (\nabla \times N \cdot \mu^{-1}\nabla \times A_e)\,dv + \int_{\Omega_e} (j\omega\sigma N A_e)\,dv$$

$$= \int_{\Omega_n} \nabla \times N \cdot H_s\,dv - \int_{\Omega_n} \frac{\mu_0}{\mu}\nabla \times N \cdot H_s\,dv - \int_{\Omega_n} N \cdot j\omega\sigma A_s\,dv, \tag{5}$$

where N is the linear combination of edge-based shape functions, Ω_e is the eddy current region and Ω_n is the current source region. The system of equations for the field modelling is complex and under-determined. Biconjugate gradient stable (Bicgstab) can be applied to solve A_e from the linear system

$$(K + j\omega C)A_e = b,$$

without applying any gauge condition. Here b is the source current density.

The sensitivity formula has been previously derived in Soleimani (2006). With the (A, A) formulation and using edge finite element, the sensitivity matrix $(\frac{\delta V}{\delta\sigma})$ of the eddy current area can be calculated using dot product of electric fields (Soleimani 2006), provided with equations $E = -j\omega A$. The sensitivity term between channels i and j for conductivity can be expressed as follows:

$$\frac{\delta V_{ij}}{\delta\sigma_k} = -\frac{\omega^2}{I_iI_j}\{A_i\}\left(\int_{\Omega_{ek}}\{N\}\cdot\{N\}^T\,dv\right)\{A_j\}^T. \tag{6}$$

Equation (6) gives us sensitivity of the induced voltage pairs V_{ij} of coils of i, j with respect to an element. Ω_{ek} is the volume of element number k and I_i and I_j are excitation currents for the sensors i and j, respectively. Figure 5(a) shows the central part of the sensitivity map for two opposite coils, which are positioned at $(+0.45, 0)$ and $(-0.45, 0)$ with a uniform distributed background of 1 S m^{-1} conductivity. Figure 5(b) shows the central part of the sensitivity map for two coils at 90°, where the coils are located at $(-0.45, 0)$ and $(0, -0.45)$, respectively.

With the new two-potential methods, forward model computation becomes faster, and the meshing process also becomes more straightforward, as coil structures do not need to be considered when creating the mesh. The calculated result from the new forward model is also promising, as the results shown in figure 5 are in strong agreement with the results reported in Soleimani et al (2005). The forward model can be further verified by comparing the experimental phase measurement and the theoretical values (the output of the forward modelling, with a given conductivity distribution). Figure 6(a) is the phase
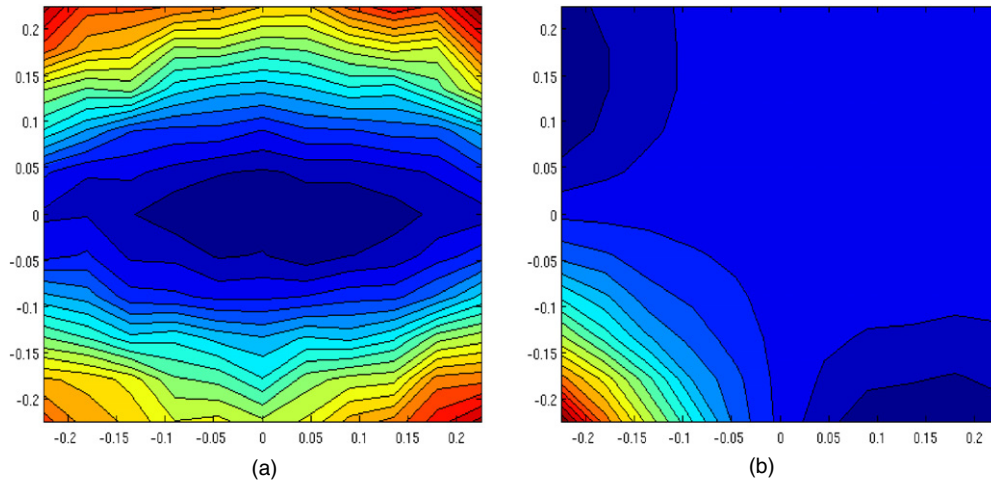
Figure 5. Sensitivity plot for (a) two opposite coils and (b) two coils at 90° in a uniform background conductivity distribution of 1 S m^{-1}.
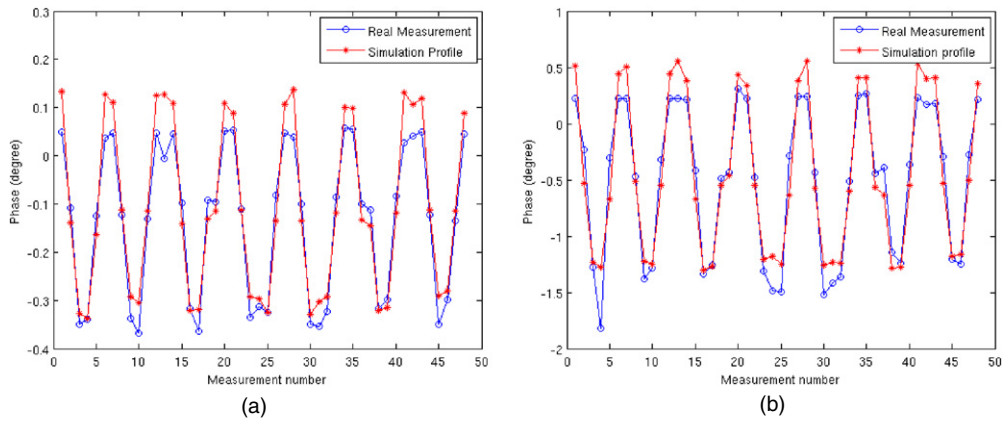

Figure 6. Theoretical and experimental phase difference comparison when inserting (a) 1% saline solution bottle into 0.9% saline solution background and (b) 5% saline solution bottle at the centre, with a 0.9% saline solution background.

difference measurement ($\text{Im}(\delta V)$) when a 1% saline bottle is inserted at the centre of the ROI, whereas figure 6(b) shows the case when a 5% saline bottle is again inserted at the centre position (corresponding to the result shown in figure 10(b)). Although some degrees of error are expected due to the discretization in Biot–Savart calculation, the plots show a reasonably good agreement between theoretical and experiment values. A complete sensor model includes an E-field shielding that can further improve the forward model accuracy but it will increase the complexity of the model and computational time.

4.2. Image reconstruction

The inverse problem for MIT is to convert the voltage measurements into a conductivity distribution image. The inverse problem in MIT is generally ill posed and nonlinear. However, solving a nonlinear problem requires extensive computation of electromagnetic fields and

updating the sensitivity maps. Therefore, in most electrical tomography cases, linear responses are often presumed when reconstructing images using inverse solvers. This linear response assumption can simplify the nonlinear problem to a linear approximation, where the problem can be solved through the matrix multiplications.

The Tikhonov regularization algorithm was selected for solving the inverse problem. Tikhonov regularization is a linear method for solving the ill-posed inverse problem with the following equation:

$$x = (J^\top J + \lambda I)^{-1} J^\top z, \tag{7}$$

where x is the pixels of the conductivity distribution, z is the normalized voltage measurements from the coil sensors, J is the Jacobian matrix (comprised by the sensitivity analysis), I is the identity matrix and λ is the regularization parameter. This single-step linear method is adapted by several groups (Ma *et al* 2006, Luis *et al* 2002, Soleimani and Lionheart 2005, Soleimani *et al* 2006). The regularization parameter was chosen empirically throughout the entire experiments.

4.3. System setup

In this initial experiment, saline solutions with different concentration: 0% ($\sigma = 0.000\,42$ S m^{-1}), 0.9% ($\sigma = 1.58$ S m^{-1}), 1% ($\sigma = 1.72$ S m^{-1}), 3% ($\sigma = 2.31$ S m^{-1}) and 5% ($\sigma = 7.26$ S m^{-1}) by weight were used to verify the biological tissue measurement capability of the MIT system. The conductivity of the saline was measured by a Mettler Toledo Conductivity meter S30 at a temperature of 23 °C. The saline solution was contained in a 6 cm diameter water bottle, forming a cylindrical column of 18 cm height. The S30 meter has a built-in temperature compensation function to counter the conductivity changes due to the temperature variation. All the measurements were completed within a relatively short period, to avoid any other source of environmental variation. For the image reconstruction experiment, the 0.9% saline bottle was placed into a freezer on purpose to decrease its conductivity. The frozen bottle will be used for the image reconstruction; a successful detection of the frozen 0.9% bottle in the same 0.9% saline conductive background can be a good indication for the future MIT application on cryo-surgery monitoring.

A two-channel measurement system (one transmitter and one receiver) was assembled to test the capability of the system for saline detection. The distance between the transmitter and the receiver is 20 cm, as shown in figure 7. Freespace background was chosen in this experiment as the sensor responses are the main focus of this test. The saline bottles were moved across the *x*-axis, and the amount of phase shift was measured at each saline bottle position. In order to obtain a stable and linear inductive response, an operational frequency of 10 MHz was selected for all of the experiments, as 10 MHz is believed to be well below the resonance frequency (45 MHz). I/Q demodulation technique was used for phase calculation because of its better accuracy and stability performance.

A 16-channel MIT system was also assembled for reconstructing the conductivity distribution images. The channel switching card NI 2593 is configured to the $2 \times 8 : 1$ multiplexer scheme; so, eight of the sensor coils were dedicated to transmitters and the other eight coils were dedicated to receivers. The transmitters and the receivers were attached in adjacent positions and evenly spread around a 23 cm diameter perspex cylinder to ensure the system's symmetry. LabView programs were used to control the data acquisition and channel switching tasks. Figure 8 shows the system's block diagram and the system setup for the saline imaging experiment.

With this setup of eight transmitters and eight receivers, a total of $8 \times 8 = 64$ measurements can be obtained to reconstruct one image. However, two measurements from the receivers that
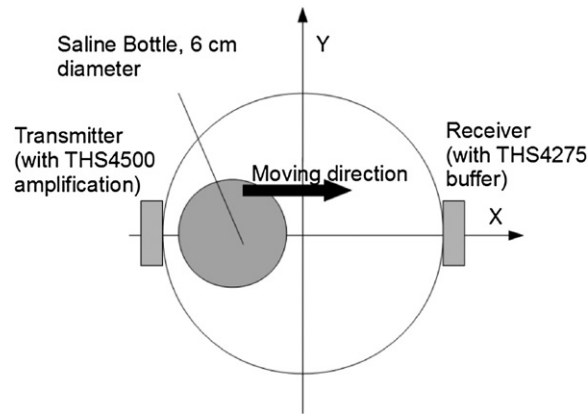
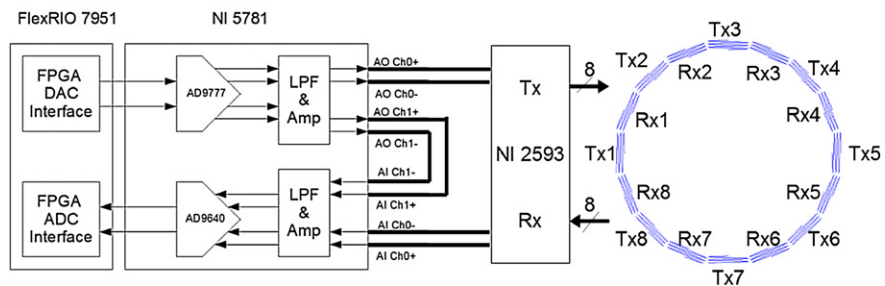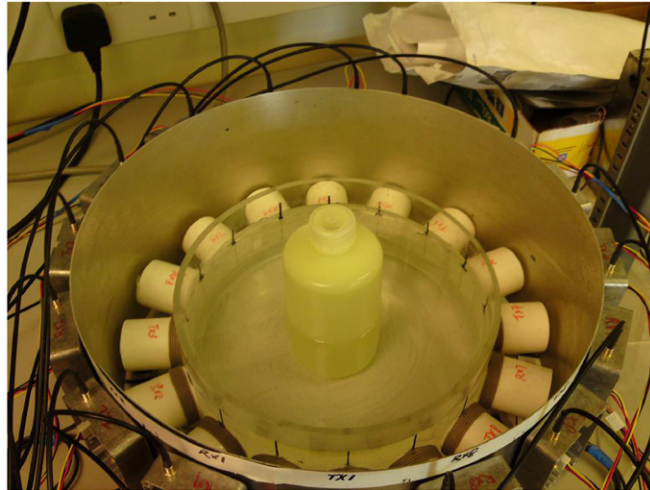**Figure 7.** The system setup for the two-channel saline measurements.

Figure 8. The complete 16-channel MIT system block diagram and the setup for saline bottle detection.

are adjacent to each transmitter need to be dropped as the induced voltages are too large to be sampled by the ADCs. Therefore, only $8 \times (8-2) = 48$ measurements are used for reconstructing one image frame. The system's background region was filled with the 0.9%
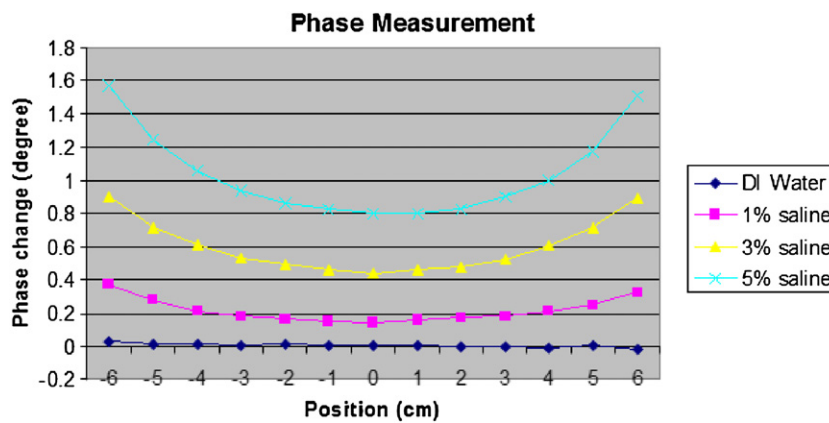
Figure 9. Phase measurement versus the saline bottle position along the *x*-axis.

medical saline solutions. Measurement voltage data would be collected when the saline bottles were placed in various places inside the measuring area. The correctness of our forward and inverse solver is validated through the accuracy of the reconstructed images.

5. Experimental result

5.1. Two-channel system result

Figure 9 shows the phase change on the receiver when different saline bottles were moved to different position along the *x*-axis. The phase shift was measured with the freespace background.

The figure shows that the sensor coil can successfully pick up the tiny phase perturbation due to the presence of the low-conductivity saline solution. The measured phase shift varies very systematically as a function along the *x*-axis, meaning that the measuring area around the sensor coils is more sensitive than the other areas. The phase shift response matches the previous sensitivity analysis result shown in figure 5(a).

5.2. Imaging results

Several experimental tests were carried out to show the capability of the new imaging system for medical MIT applications. The 16-channel full MIT system was tested with the frozen 0.9% (non-conductive), 3% and 5% saline solutions, with the 0.9% saline solution as the conductive background. It should be noted that the saline used to simulate the biomedical samples has a slightly higher conductivity than real tissue. However, the tests were still considered adequate to show the performance of the MIT system and provided further insight into MIT with its potential medical applications in the future, such as lung imaging and cryo-surgery monitoring. Figure 10 shows the imaging results of the saline solutions using the image reconstruction algorithms described in the previous section.

For image accuracy comparison, the size, location and shape of the saline bottles are marked in the images with dashed lines. The image qualities such as ringing effect (RNG) and resolution (RES) are then further quantified using the GREIT standard (Adler *et al* 2009). RES measures the ratio of simulated image pixel amplitudes to the total image pixel amplitude; the result is then divided by the true ratio. The RES value would equal 1 in an ideal case. RNG
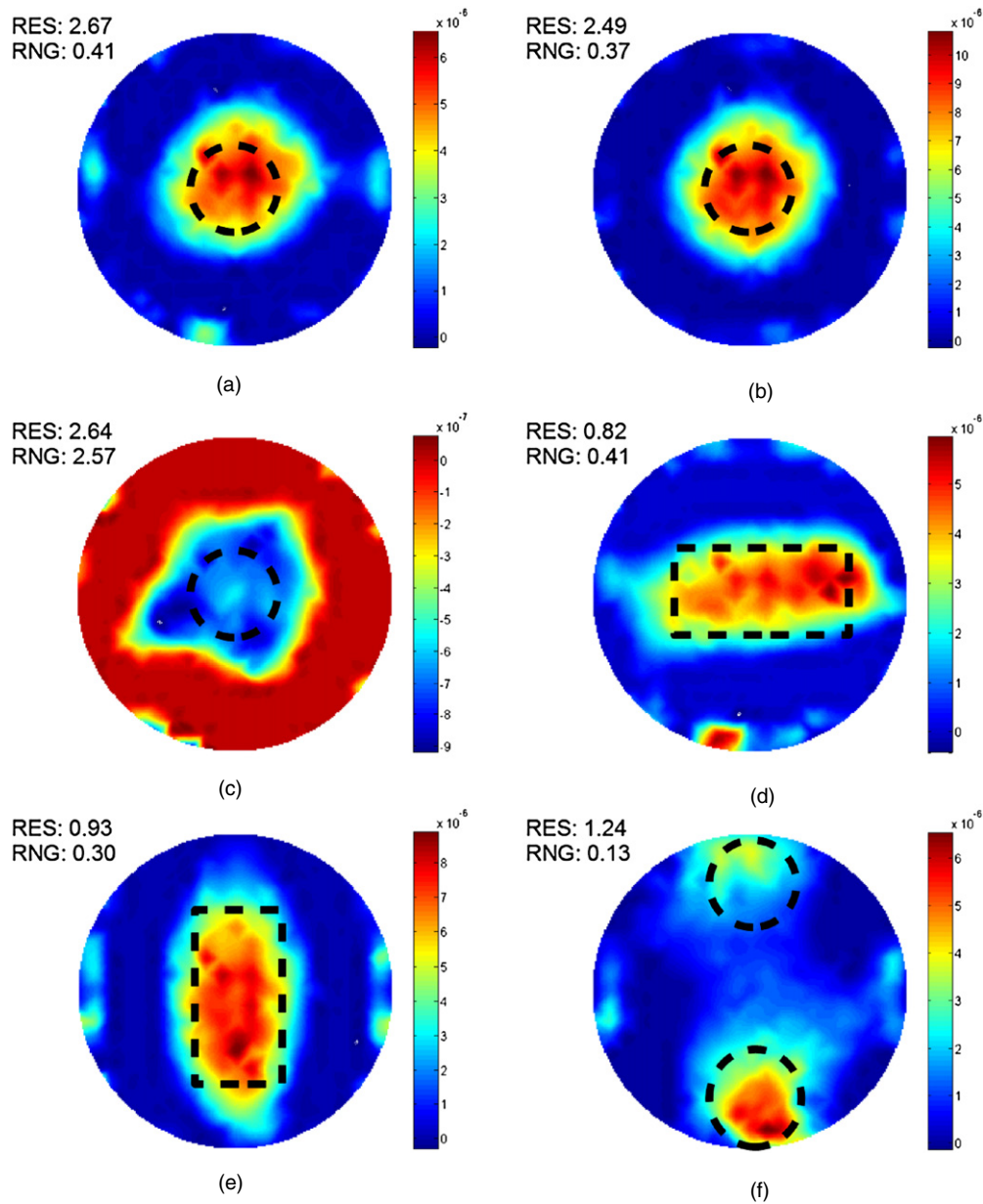
Figure 10. Reconstructed images of salines bottles, (a) 3% bottle at the centre, (b) 5% bottle at the centre, (c) frozen 0.9% bottle at the centre, (d) 3% saline bottle in horizontal position, (e) 5% saline bottle in vertical position and (f) 5% bottle at the bottom and 3% bottle at the top.

measures whether the area surrounding the main measuring target in the reconstructed image has a RNG; the larger the value, the greater the RNG.

In the single object cases (figures 10(a)–(c)), the location of the image is well reconstructed when the saline bottles are inserted at the centre. The concentration of the saline can also be determined in the image by looking at the scale bar at the right-hand side of the images.

When the inserted object has a higher conductivity (i.e. higher conductivity difference), the corresponding pixel values in the images will have higher magnitudes. It is observed that all the RES values are larger than expected for the single object experiments, i.e. the size of the reconstructed object is larger than the true size. This phenomenon is due to the poorer sensitivity at the centre area of the ROI and the effect of the regularization.

It is worth noting the negative contrast case in figure 10(c). In theory, ice should act as an insulator (no free ions for conducting electricity). Therefore in this case the inserted object has a lower conductivity than the background. This negative contrast is also correctly shown at the scale bar in figure 10(c). In figures 10(d) and (e), the saline bottle was placed 90° tilted. The shapes of the bottle are again correctly represented in the images, with better RES values that are closer to 1. In the dual-object cases (figure 10(f)), the 3% and 5% bottles can also be distinguished clearly in the figure, with correct locations. The RES performance here is more sensible than the single object cases since the saline bottles are placed at a more sensitive region of the imaging system.

The RNG is considered to be large when the objects are placed at the centre (figures 10(a)–(e)), especially in the frozen saline experiments. The small conductivity difference is believed to be the main cause, which can worsen the stability of the images. The RNG decreases in the dual object experiments, as the objects are placed in the regions near the coils that are more sensitive. Nevertheless, the RNG can be compensated by thresholding the image.

6. Conclusion

This paper presents a hardware and software framework development of an NI-based MIT system. The study has shown a preliminary characterization for our NI hardware. From the system performance result in section 3, it is shown that the NI devices can offer a stable platform that is capable of measuring phase difference down to millidegree ranges, provided that the detected signal is large enough. Furthermore, it is noted that the quadrature (I/Q) demodulation method offers much better measurement stability than the FFT tone measurement technique, and FFT tone measurement has a better phase linearity performance. These results demonstrated that a full working MIT system can be constructed using off-the-shelf NI hardware and LabView program.

From the saline experimental result, it shows that the MIT sensors are able to detect objects with conductivity less that $10\,S\,m^{-1}$. Different concentrations of saline solutions (i.e. different conductivities) can be distinguished clearly from the amount of the phase shift perturbation observed at the receiver coil. From the result obtained in figure 9, the maximum phase shift is around 1.6°, which occurs when the saline bottle is closest to the transmitter and receiver. The forward algorithms have been improved from the previous model by eliminating the coil mesh, which can effectively increase the system's flexibility. The Tikhonov inverse technique also shows promising results via its reconstructed images. The images can correctly represent the location, the shape and the conductivity of the inserted objects.

At this stage most of the data acquisition time is spent on data transferring from the FPGA chip to the PC, as all the data stored in the FPGA chip need to be sent to the work station for signal processing (I/Q demodulation). However, it is believed that the system's real-time performance can be increased further by utilizing the NI FPGA's mathematical library to handle some of the signal processing tasks. In this case the amount of data needed to be transferred to the work station can be decreased significantly; hence, the 'bottleneck' can be avoided. The ongoing work of system development will therefore be the FPGA module development in LabView, and also the development of the multi-frequency methods which can potentially provide more information for complex biomedical samples. Different inverse algorithms will

also be studied to achieve a faster image reconstruction process. A dedicated biomedical application for MIT will be necessary for the next step of the hardware modification. For example, if the system is going to be applied in an unstable temperature environment, the IC chip on the receiver board might need to be replaced by an AD8099 for better temperature stability.

References

Adler A *et al* 2009 GREIT: a unified approach to 2D linear EIT reconstruction of lung images *Physiol. Meas.* **30** S35–55

Biro O 1999 Edge element formulations of eddy current problems *Comput. Methods Appl. Mech. Eng.* **169** 391–405

Biro O and Preis J 1989 On the use of the magnetic vector potential in the finite element analysis of three-dimensional eddy currents *IEEE Trans. Magn.* **25** 3145–59

Biro O and Preis K 2000 An edge finite element eddy current formulation using a reduced magnetic and a current vector potential *IEEE Trans. Magn.* **36** 3128–30

Griffiths H 2001 Magnetic induction tomography *Meas. Sci. Technol.* **12** 1126–31

Griffiths H, Gough W, Watson S and Williams R J 2007 Residual capacitive coupling and the measurement of permittivity in magnetic induction tomography *Physiol. Meas.* **28** S301–11

Kameari A 2004 Regularization on ill-posed source terms in fem computation using two magnetic vector potentials *IEEE Trans. Magn.* **40** 1310–3

Korjenevsky A, Cherepenin V and Sapetsky S 2000 Magnetic induction tomography: experimental realization *Physiol. Meas.* **21** 89–94

Luis R C, da Silva A F and Borges A R 2002 Magnetic induction tomography imaging using Tikhonov regularization *Workshop on Inverse Obstacle Problems (Lisbon)*

Ma X, Peyton A J, Higson S R, Lyons A and Dickinson S J 2006 Hardware and software design for an electromagnetic induction tomography (EMT) system applied to high contrast metal process applications *Meas. Sci. Technol.* **17** 111–8

McEwan A L, Hamsch M, Watson S, Igney C H and Kahlert J 2009 A comparison of two phase measurement techniques for magnetic impedance tomography *IFMBE Proc. World Congress on Medical Physics and Biomedical Engineering* vol 25/2 pp 4–6

Patz R, Watson S, Ktistis C, Hamsch M and Peyton A J 2010 Performance of a FPGA-based direct digitising signal measurement module for MIT *(Int. Conf. on Electrical Bioimpedance) J. Phys.: Conf. Ser.* **224** 012017

Rosell-Ferrer J, Merwa R, Brunner P and Scharfetter H 2006 A multifrequency magnetic induction tomography system using planar gradiometers: data collection and calibration *Physiol. Meas.* **27** S271–80

Scharfetter H, Kostinger A and Issa S 2008 Hardware for quasi-single-shot multifrequency magnetic induction tomography (MIT): the Graz Mk2 system *Physiol. Meas.* **29** S431–43

Scharfetter H, Lackner H K and Rosell J 2001 Magnetic induction tomography: hardware for multi-frequency in biological tissue *Physiol. Meas.* **22** 131–46

Scharfetter H, Merwa R and Pilz K 2005 A new type of gradiometer for the receiving circuit of magnetic induction tomography *Physiol. Meas.* **26** S307–18

Soleimani M 2006 Sensitivity maps in three-dimensional magnetic induction tomography *Insight, Non-Destr. Test. Cond. Monit.* **48** 39–44

Soleimani M and Lionheart W R B 2005 Image reconstruction in three-dimensional magnetostatic permeability tomography *IEEE Trans. Magn.* **41** 1274–9

Soleimani M, Lionheart W R B, Peyton A J and Ma X 2005 A 3D inverse finite element technique applied to experimental magnetic induction tomography data *Proc. 4th World Congress on Industrial Process Tomography (Aizu, Japan)* pp 1054–9

Soleimani M, Lionheart W R B, Peyton A J, Ma X and Higson S R 2006 A three-dimensional inverse finite-element method applied to experimental eddy-current imaging data *IEEE Trans. Magn.* **42** 1560–7

Vauhkonen M, Hamsch M and Igney C H 2008 A measurement system and image reconstruction in magnetic induction tomography *Physiol. Meas.* **29** S445–54

Watson S 2009 Instrumentation for low-conductivity magnetic induction tomography *PhD Thesis* University of Glamorgan, United Kingdom

Watson S, Wee H C, Griffiths H and Williams R J 2011 A highly phase-stable differential detector amplifier for magnetic induction tomography *Physiol. Meas.* **32** 917–26

Watson S, Williams R J, Griffiths H, Gough W and Morris A 2001 A transceiver for direct phase measurement magnetic induction tomography *Proc. 23rd Annu. Int. Conf. of the IEEE Engineering in Medicine and Biology Society,* pp 25–27

Watson S, Williams R J, Griffiths H, Gough W and Morris A 2003 Magnetic induction tomography: phase versus vector–voltmeter measurement techniques *Physiol. Meas.* **24** 555–64

Watson S, Williams R J, Gough W A and Griffiths H 2008 A magnetic induction tomography system for samples with conductivities less than 10 S m^{-1} *Meas. Sci. Technol.* **19** 045501

Wee H C, Watson S, Patz R, Griffiths H and Williams R J 2008 A magnetic induction tomography system with sub-millidegree phase noise and high long-term phase stability *Proc. 4th European Conf. of the Int. Federation for Medical and Biological Engineering* **22** 744–7

Wei H Y and Wilkinson A J 2011 Design of a sensor coil and measurement electronics for magnetic induction tomography *IEEE Trans. Instrum. Meas.* **60** 3853–9

Yin W, Chen G, Chen L and Wang B 2011 The design of a digital magnetic induction tomography (MIT) system for metallic object imaging based on half cycle demodulation *IEEE Sensors J.* **11** 2233–40